Volume 26
Number 39
21 October 2024
Pages 25253–25734

# PCCP

Physical Chemistry Chemical Physics

rsc.li/pccp

25 YEARS ANNIVERSARY

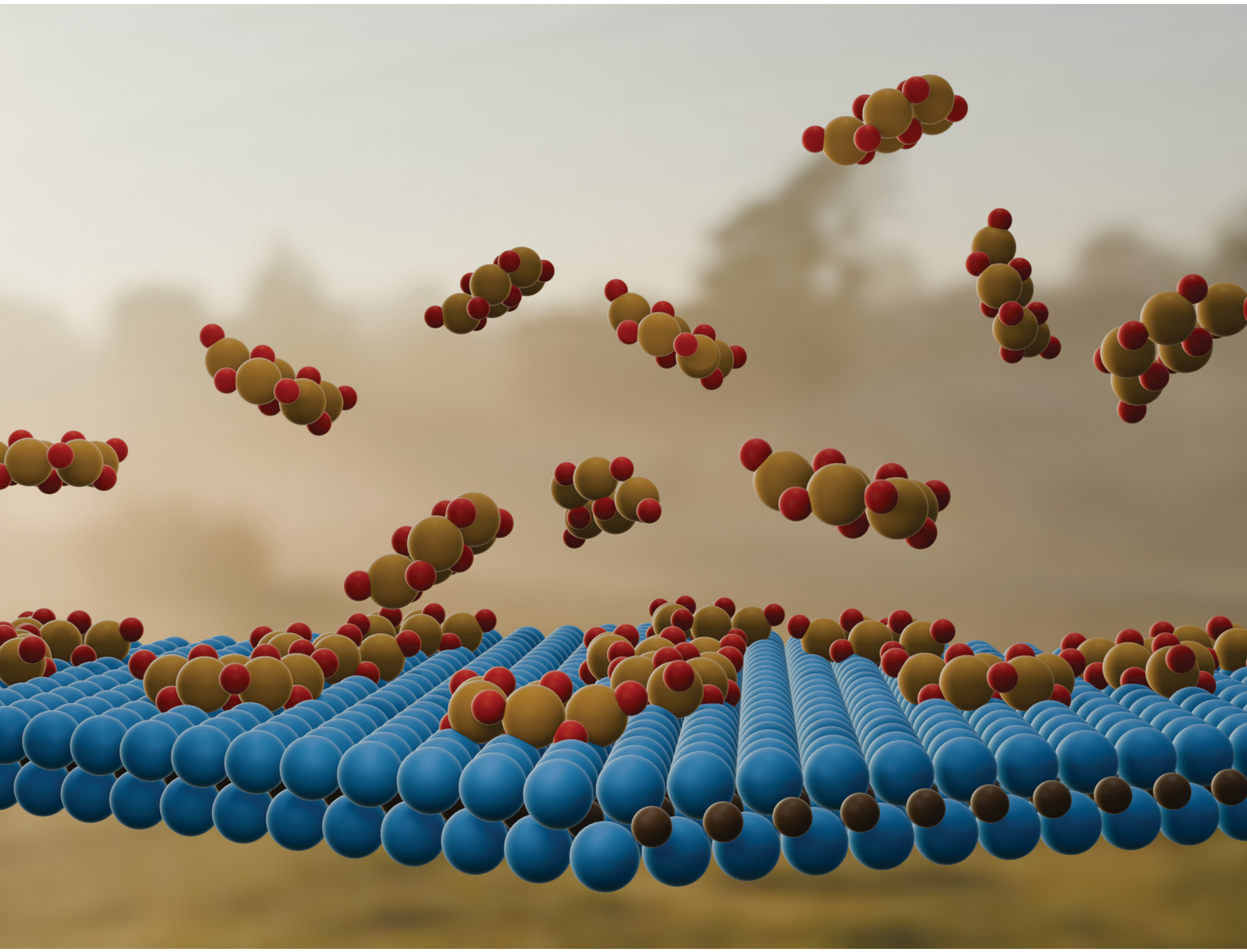

ISSN 1463-9076

ROYAL SOCIETY OF CHEMISTRY

**PAPER**

Ángel Morales-García *et al.*

First principles modeling of composites involving $TiO_2$ clusters supported on $M_2C$ MXenes

PCCP Owner Societies

PCCP

PAPER

View Article Online
View Journal | View Issue

Check for updates

Cite this: *Phys. Chem. Chem. Phys.*, 2024, **26**, 25319

# First principles modeling of composites involving $TiO_2$ clusters supported on $M_2C$ MXenes†

Masoomeh Keyhanian, ‡[a] Néstor García-Romeral, ‡[b] Ángel Morales-García, *[b] Francesc Viñes [b] and Francesc Illas [b]

First-principles calculations based on density functional theory are performed to investigate the formation of titania/MXene composites taking $(TiO_2)_5/M_2C$ (M = Ti, Zr, Hf, V, Nb, Ta, Cr, Mo, and W) as cases of study. The present systematic analysis confirms a favorable, high exothermic interaction, which promotes important structural reconstructions of the $(TiO_2)_5$ cluster along with charge transfer from the MXene to titania. MXenes composed of $d^3$ transition metals promote the strongest interaction, deformation energy, and charge transfer, followed by $d^4$ and $d^5$ $M_2C$ MXenes. We provide evidence that the formation of these $(TiO_2)_5/M_2C$ composites is governed by charge transfer, leading to scaling relationships. By using the electronegativity of the metal composing MXene and the MXene d-band center, we also establish linear correlations that can be used to predict the interaction strength of $(TiO_2)_5/M_2C$ composites just from the knowledge of the MXene composition. It is likely that the present trends hold for other $TiO_2$/MXene composites.

Received 28th April 2024,
Accepted 19th July 2024

DOI: 10.1039/d4cp01757a

rsc.li/pccp

Open Access Article. Published on 22 July 2024. Downloaded on 7/9/2025 8:47:37 PM.
This article is licensed under a Creative Commons Attribution-NonCommercial 3.0 Unported Licence.

## 1. Introduction

During recent decades, the relationship between semiconducting transition metal oxides (TMOs) and photocatalysis has been a topic of high interest in the scientific community, especially since the seminal paper published by Fujishima and Honda in 1972.[1] Shortly, a photon of appropriate energy, ideally from sunlight, can be used to activate a catalyst generating electron–hole pairs to drive redox reactions.[2,3] This solar-to-chemical energy transformation induced by semiconducting materials forms the basis of the so-called heterogeneous photocatalysis which plays an important role in a broad range of applications including microorganism inactivation, degradation of pollutants, water splitting, or $CO_2$ photoreduction among others.[4–7] Different semiconducting materials such as $WO_3$, ZnO and $TiO_2$ have been investigated as suitable photocatalysts, with the latter being the most broadly studied candidate.[8–11] However, the full potential of this technology is still limited because of the too wide band gap of these materials—3.0 to 3.2 eV in the case of $TiO_2$—and fast electron–hole recombination. These drawbacks seriously limit the activation of the semiconductor under sunlight and promote low photoactivity.[12–14]

One proven strategy to enhance the photoactivity of a semiconductor is to integrate a new component. This is expected to facilitate charge carriers' separation by forming an interface with the semiconducting photocatalyst. Also, the new component can participate as an active site for the surface reaction. Experimental and computational studies have proposed both metals (Pt, Pd, Ru, Ag, and Au)[15–19] and non-metals (C and N)[19–22] as new constituents to anchor over or dope nanostructured $TiO_2$ materials. The resulting systems show relative photocatalytic activity improvement due to the longer charge carrier lifetimes. In this quest for robust photocatalysts with superior charge carrier separation, low dimensional carbides and/or nitrides (called MXenes)[23] appear as suitable candidates to generate hybrid catalysts together with TMOs to overcome the aforementioned limitations.[24]

MXenes exhibit a $M_{n+1}X_nT_x$ general chemical formula where M stands for early transition metals, X corresponds to carbon and/or nitrogen elements, and $T_x$ represents the terminal groups of MXene (*i.e.*, OH, H, O, or F) derived from the top-down synthesis taking MAX phases as a precursor. Finally, *n* denotes the thickness of the MXene in terms of atomic layers and runs from 1 to 3. MXenes have shown to be versatile materials in a broad landscape of applications, including catalysis.[25–30] In the realm of photocatalysis, a series of photoactive MXene-based compounds have been proposed as promising photocatalysts for efficient $CO_2$ reduction, and $H_2$ generation through water splitting.[24,31–33]

[a] *Department of Physical Chemistry, Faculty of Chemistry, University of Mazandaran, Babolsar 47416-95447, Iran*
[b] *Departament de Ciència de Materials i Química Física & Institut de Química Teòrica i Computacional (IQTCUB), Universitat de Barcelona, c/Martí i Franquès 1-11, 08028 Barcelona, Spain. E-mail: angel.morales@ub.edu*

† Electronic supplementary information (ESI) available: Tables S1–S12 and Fig. S1 and S2. See DOI: https://doi.org/10.1039/d4cp01757a

‡ Equally contributed.

Open Access Article. Published on 22 July 2024. Downloaded on 7/9/2025 8:47:37 PM.
This article is licensed under a Creative Commons Attribution-NonCommercial 3.0 Unported Licence.

Concerning $TiO_2$/MXene composites, several experimental studies have been reported.[34–38] These studies show that the use of MXenes as co-catalysts could improve the photocatalytic activity compared to the use of isolated semiconductors as titania. One important aspect of such improvement resides in the interface contact type between both cocatalysts. A Schottky barrier formed at the interface prevents the back diffusion of the electrons, thus, preventing charge recombination of photogenerated electrons.

Instead of these reports, the interfacial structure and electronic properties of these composites remain largely unknown. Thus, theoretical analyses are necessary to identify and rationalize the structural and electronic aspects that could contribute to the enhancement of catalytic performance,[39] and prior further theoretical studies regarding their reactivity in heterogeneous or photocatalytic reactions on these systems can be undertaken. Using extended periodic models, Xu and coauthors investigated the interfacial properties of $Ti_{n+1}C_nT_x/TiO_2$ ($n$ = 1, 2) heterostructures including O, OH, and F as $T_x$ termination, and selected the (101) surface to represent the slab model of anatase $TiO_2$.[40] This study revealed the strong dependence of the interfacial interaction and properties of the $TiO_2$/MXene heterostructures on the surface composition of the MXene. One step further was recently carried out by us investigating the $TiO_2$/MXene composites but considering nanostructured $TiO_2$ systems, $(TiO_2)_5$ and $(TiO_2)_{10}$ clusters, supported on a bare $Ti_2C$ surface.[41] A remarkable exothermic interaction was reported, accompanied by significant deformation of the adsorbed titania clusters and substantial charge transfer from the MXene towards the $TiO_2$ clusters. Nevertheless, all the heterostructures described so far, both theoretically and experimentally, involved only Ti-based MXenes as the substrate and a comprehensive study comparing the effect of other transition metals composing MXenes on the supported $TiO_2$ cluster is missing. Thus, we focus here on a systematic computational analysis to gain further knowledge of the effects of MXene composition on the structural and electronic properties of $TiO_2$/MXene composites. To this end, we select bare $M_2C$ (0001) MXenes (M = Ti, Zr, Hf, V, Nb, Ta, Cr, Mo, and W) as substrates to support a $(TiO_2)_5$ cluster.

## 2. Computational details

The influence of MXene composition when forming $TiO_2$/MXene composites was investigated by considering extended $M_2C$ (M = Ti, Zr, Hf, V, Nb, Ta, Cr, Mo, and W) MXene slabs exposing the (0001) surface with ABC stacking as depicted in Fig. 1. From a synthetic point of view, MXenes are generated using a top-down procedure using MAX phases as precursors. This involves chemical etching of the A-element in the MAX phase and further sonication to separate the generated MXenes exposing the basal (0001) surface. The $(TiO_2)_5$ titania cluster was selected as a representative example to study the interaction with the different MXene surfaces. The $(TiO_2)_5$ cluster was chosen as it provides a good representative model for experimental composites and a suitable theoretical case to study the chemical bonding in these systems. This selection was based on previous work on the $(TiO_2)_5/Ti_2C$ composite[41] which constitutes an appropriate guide to compare both studies. The atomic structure of the gas phase $(TiO_2)_5$ cluster used as a reference was obtained using global optimization methods and exhibits the lowest energy in the potential energy surface (PES), see Fig. 1.[42,43] An efficient analysis of the interacting landscape was carried out by generating different conformations by rotating the $(TiO_2)_5$ nanocluster over the $M_2C$ (0001) MXene surfaces. This screening procedure where a rotational angle $\alpha$ covers a 140° range with a step of 10° and guarantees a thorough assessment of PES attending to the inherent hexagonal symmetry exposed by the MXene slab models. Further details are described in ref. 41.

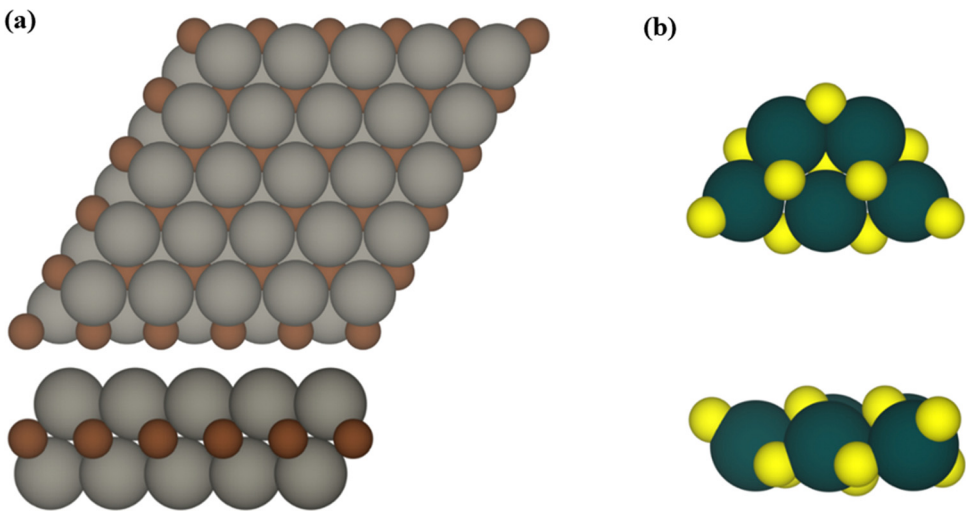


Fig. 1 Top (top) and side (bottom) views of (a) the $p(5 \times 5)$ supercell model of the (0001) $M_2C$ MXene structure with an ABC stacking and (b) planar $(TiO_2)_5$ cluster. Gray and brown spheres represent transition metal M (M = Ti, Zr, Hf, V, Nb, Ta, Cr, Mo, and W) and C atoms in the $M_2C$ (0001) MXene surface, while yellow and dark green spheres stand for oxygen and titanium atoms of the titania cluster, respectively.

 This journal is © the Owner Societies 2024

Open Access Article. Published on 22 July 2024. Downloaded on 7/9/2025 8:47:37 PM.
This article is licensed under a Creative Commons Attribution-NonCommercial 3.0 Unported Licence.

The structural, electronic, and bonding properties of the $(TiO_2)_5/M_2C$ composites were investigated using periodic density functional theory (DFT) based calculations as implemented in the Vienna *Ab Initio* simulation package (VASP).[44,45] Here, the Kohn–Sham equations are numerically solved using a plane wave basis set to expand the valence electron density with a kinetic energy cut-off of 415 eV. To account for the interaction between the core and valence electron density, the projector augmented wave (PAW) method was used.[46] The generalized gradient approximation (GGA) Perdew–Burke–Ernzerhof (PBE) exchange correlation density functional was selected to pursue the geometry optimizations.[47] PBE stands out as a widely recognized and broadly used DFT functional in computational materials science for its ability to accurately depict metallic systems, so it effectively characterizes the structural parameters of MXenes. To properly study the $(TiO_2)_5/M_2C$ composites, a $p(5\times5)$ $M_2C$ MXene supercell was selected as it is sufficiently large to minimize the lateral interactions between the periodically repeated titania clusters. A vacuum space of 18 Å along the direction normal to the MXene (0001) surface was included to prevent artificial electrostatic interactions between interleaved composite replicas. Given the rather large size of this supercell, calculations were carried out at the $\Gamma$ $k$-point only.[48] The convergence threshold for the electronic self-consistent field (SCF) calculations was established at $10^{-5}$ eV, and the structural optimization was reached when atomic forces were below $10^{-2}$ eV Å$^{-1}$.

First, we analyzed the thermodynamic stability of the $(TiO_2)_5/M_2C$ (M = Ti, Zr, Hf, V, Nb, Ta, Cr, Mo, and W) composites based on the adsorption energy, $E_{ads}$. This provides a measure of the exothermicity arising from supporting the $(TiO_2)_5$ cluster over the MXene (0001) surface, and is defined as:

$$E_{ads} = E_{(TiO_2)_5/M_2C} - E_{M_2C} - E_{(TiO_2)_5}, \quad (1)$$

where $E_{(TiO_2)_5/M_2C}$, $E_{M_2C}$, and $E_{(TiO_2)_5}$ correspond to the total energies of the $(TiO_2)_5/M_2C$ composite, the bare (0001) $M_2C$ MXene, and the gas phase $(TiO_2)_5$ cluster, respectively. Accordingly, $(TiO_2)_5/M_2C$ composite is thermodynamically stable when $E_{ads} < 0$. Dispersion corrections were not considered because the interaction is clearly dominated by much stronger chemical interactions, as already discussed[41] and also commented on later.

The composite formation induces a deformation of its (0001) $M_2C$ MXene and $(TiO_2)_5$ cluster components relative to their isolated configurations, and this energy cost is compensated by the interaction strength, leading to the adsorption process. Therefore, one can define the deformation energy, $E_{def}$, of either $M_2C$ or $(TiO_2)_5$, and adhesion energy, $E_{adh}$, all defined as;

$$E_{def(X)} = E_X^{sp} - E_X, \quad (2)$$

$$E_{adh} = E_{ads} - E_{def(TiO_2)} - E_{def(Ti_2C)}, \quad (3)$$

where $E_X^{sp}$ stands for the energy of the adsorbed geometry of X = $M_2C$ or $(TiO_2)_5$ systems, and $E_X$ represents the energy of the isolated components, as defined in eqn (1). The $E_X^{sp}$ term is obtained from a single-point (sp) calculation at the geometry at the adsorbed conformation removing the other component. On one hand, the $E_{def(X)}$ describes the energy required to deform any of the involved systems from its optimal structure, while, on the other hand, $E_{adh}$ quantifies the interaction strength between the deformed fragments, bonded in a lock-key fashion. The more negative $E_{adh}$ is, the stronger the interaction.

Furthermore, a topological analysis of the electron density was carried out based on the quantum theory of atoms-in-molecules proposed by Bader,[49] using the VASP-linked code developed by Henkelman *et al.*[50] The charge transfer analysis was carried out by quantifying the total number of electrons in each structure in its gas phase and composite conformations. Furthermore, the charge density difference (CDD), and its plane-averaged (PA-CDD) counterpart along the normal direction were also computed as:

$$\Delta\rho = \rho_{(TiO_2)_5/M_2C} - \rho_{M_2C} - \rho_{(TiO_2)_5}, \quad (4)$$

Table 1 Adsorption ($E_{ads}$), adhesion ($E_{adh}$), and deformation ($E_{def}$) energies (in eV) of $(TiO_2)_5/M_2C$ composites, respectively. Note that the two $E_{def}$ different sets of data correspond to the $M_2C$ (0001) MXene surface and the $(TiO_2)_5$ cluster, respectively. Charge transfer of $(TiO_2)_5$, $\Delta Q$, given in $e$, and the work function of $M_2C$, $\Phi$, given in eV, are also included. Only the most stable composite atomic configuration is included, represented by the largest $E_{ads}$. Further details are found in the ESI

| $M_2C$ | $E_{ads}$ | $E_{adh}$ | $E_{def}$ $M_2C$ | $E_{def}$ $(TiO_2)_5$ | $\Delta Q$ | $\Phi$ |
|---|---|---|---|---|---|---|
| $Ti_2C$ | −16.76 | −36.95 | 2.21 | 17.98 | −6.02 | 4.34 |
| $Zr_2C$ | −16.78 | −36.03 | 1.06 | 18.19 | −6.08 | 4.09 |
| $Hf_2C$ | −16.99 | −37.06 | 0.89 | 19.18 | −6.62 | 4.29 |
| $V_2C$ | −13.47 | −27.89 | 0.71 | 13.71 | −4.15 | 4.40 |
| $Nb_2C$ | −13.08 | −23.48 | 0.91 | 9.49 | −3.53 | 4.26 |
| $Ta_2C$ | −14.11 | −25.40 | 1.09 | 10.19 | −3.66 | 4.59 |
| $Cr_2C$ | −12.59 | −24.95 | 1.57 | 10.79 | −3.48 | 4.71 |
| $Mo_2C$ | −10.12 | −18.52 | 1.03 | 7.37 | −2.34 | 4.99 |
| $W_2C$ | −10.37 | −17.62 | 1.76 | 5.49 | −2.04 | 4.93 |

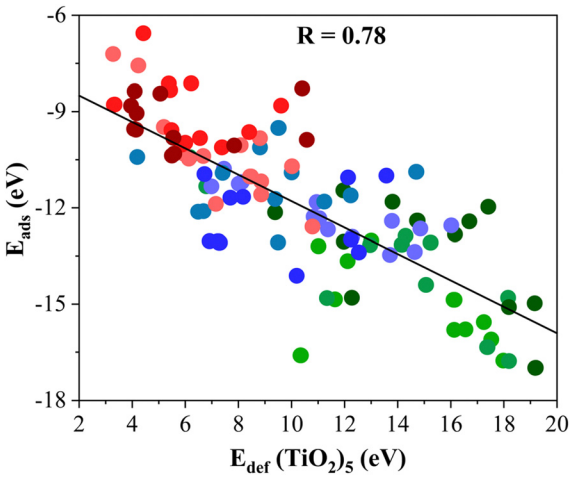


Fig. 2 Linear trend between the $E_{ads}$ of $(TiO_2)_5/M_2C$ composites and $E_{def}$ $(TiO_2)_5$. The solid black line is the linear correlation between both quantities where R stands for the regression coefficient between them. The spheres colors are consistent with the colored spheres of the metal atom in the MXene surface, depicted in Fig. 3. Linear fitting analysis is reported in Table S12 of the ESI.†

Open Access Article. Published on 22 July 2024. Downloaded on 7/9/2025 8:47:37 PM.
This article is licensed under a Creative Commons Attribution-NonCommercial 3.0 Unported Licence.

where $\Delta\rho$ corresponds to the CDD while, $\rho_{(TiO_2)_5/M_2C}$, $\rho_{M_2C}$, and $\rho_{(TiO_2)_5}$ represent the charge density of $(TiO_2)_5/M_2C$, $M_2C$, and $(TiO_2)_5$, respectively. The analysis of the chemical bond *via* CCD and PA-CCD provides an eye-catching view of the electron transfer between the components constituting the titania/MXene composites. The command-line VASPKIT program[51] was used to determine the work function, $\Phi$, for bare $M_2C$ MXenes, which involves subtracting the Fermi energy value, $E_F$, from the electrostatic average potential energy in the vacuum. Finally, additional test caluclations with spin polarization showed that the magnetica moment in $Ti_2C$, $Zr_2C$, and $Hf_2C$ composites vanishes which is in line with results the O- or OH-terminated MXenes.

## 3. Results and discussion

We start this section by discussing in detail the trends of energetic features, *i.e.*, adsorption, adhesion, and deformation energies. Next, we continue with the rationalization of these properties based on the chemical bonding analysis as the charge transfer, the CCD and PA-CDD. Finally, we will propose

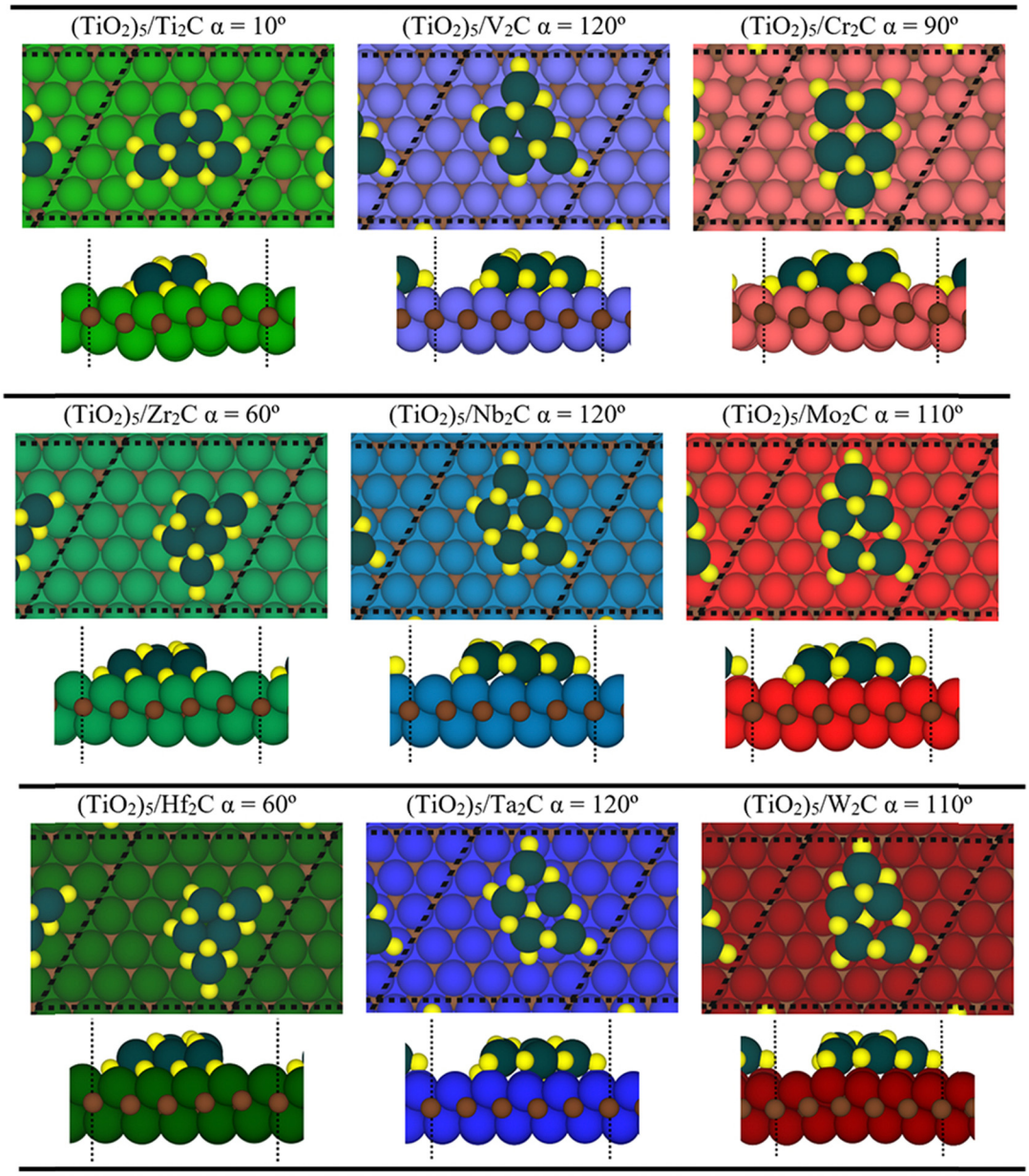


Fig. 3 Top (top) and side (bottom) views of the optimized geometries of $p(5\times5)$ (dashed black line) $(TiO_2)_5/M_2C$ composite structures. Note that these structures correspond to the most stable configuration for each $(TiO_2)_5/M_2C$. The color scheme of the C atom and $(TiO_2)_5$ cluster is the same as in Fig. 1. The green, blue, and red colors denote M atoms of groups IV, V, and VI, respectively, where light, solid, and darker shades imply 3d, 4d, or 5d series, respectively.

 This journal is © the Owner Societies 2024

Open Access Article. Published on 22 July 2024. Downloaded on 7/9/2025 8:47:37 PM.
This article is licensed under a Creative Commons Attribution-NonCommercial 3.0 Unported Licence.

useful scaling relationships allowing one to establish the structural and bonding properties that govern the formation of titania/MXene composites.

### 3.1. Energetic stability of $(TiO_2)_5/M_2C$ composites

Exploration of the potential energy surface (PES) of $(TiO_2)_5/M_2C$ systems is carried out by computing the interaction energy, this is, the $E_{ads}$, between the $(TiO_2)_5$ nanocluster over the $p(5\times5)$ $M_2C$ (M = Ti, V, Cr, Zr, Nb, Mo, Hf, Ta, and W) MXene supercell (*cf.* Fig. 1). This interacting process is systematically simulated by rotating the $(TiO_2)_5$ nanocluster over each $M_2C$ (0001) surface by varying the rotational angle as mentioned above, following a previous scheme recently used in the analysis of $(TiO_2)_n/Ti_2C$ ($n$ = 5 and 10) and titania/titania interfaces.[41,52] Due to the hexagonal symmetry of the MXene, analogous interacting conformations are expected to be found by shifting the titania cluster in the *xy* plane. See the ESI† for further details.

Table 1 compiles the computed energy values defined by eqn (1)–(3) for the most stable configuration of each $(TiO_2)_5/M_2C$ composite. To avoid misunderstanding, we focus initially on the most stable configurations taking the most exothermic cases (*i.e.*, largest $E_{ads}$) for each composite (*cf.* Table 1). The complete analysis for all plausible conformations in each MXene surface is listed in Tables S1–S9 of the ESI.† First, $E_{ads}$ indicates an exothermic interaction ranging from −10.12 to −16.99 eV. The composition of the MXene surface promotes different adsorption energies. Indeed, the formation of $(TiO_2)_5/M_2C$ composites is the most exothermic over an MXene surface involving $d^3$ transition metals (M = Ti, Zr, and Hf) with $E_{ads}$ values of −16.76, −16.78, and −16.99 eV, respectively. On the other hand, we find MXene surfaces composed of $d^5$ transition metals (M = Cr, Mo, and W) expose the lowest, yet quite large, exothermicity with $E_{ads}$ values of −12.59, −10.12, and −10.37 eV, respectively. Finally, the MXenes composed of $d^4$ transition metals (M = V, Nb, and Ta) present $E_{ads}$ values with energies between both extremes with values of −13.47, −13.08, and −14.11 eV, respectively. Attending to the location of the transition metal in the periodic table, one can capture some trends in $E_{ads}$. In turn, the adsorption energy becomes less favorable when moving through the period. This indicates that the MXene surface reduces its reactivity with the titania cluster as the number of d electrons increases. This is consistent with the trends reported when $M_2C$ MXenes are used as template generating single-atom catalysts (SACs).[53]

The $E_{adh}$ follows a similar trend as $E_{ads}$, see Table 1, running from −17.62 to −37.06 eV. Again, the most reactive MXenes are those involving $d^3$ metals with the largest $E_{adh}$ followed by $d^4$ and $d^5$ metal ones. In turn, this adhesion energy is directly related to the deformation energy ($E_{def}$) of the $(TiO_2)_5$ cluster and the $M_2C$ (0001) surface that takes place during the formation of titania/MXene composites as listed in Table 1. Here, one can readily see that the formation of $(TiO_2)_5/M_2C$ composites affects in a different way to the structural framework of each constituent. Starting with the $M_2C$ (0001) MXene surface, its $E_{def}$ is relatively low and ranges in value between 2.21 and 0.71 eV only. On the other hand, one can see that this $E_{def}$ is significantly larger for the $(TiO_2)_5$ nanocluster with values encompassing values between 5.49 and 19.18 eV. Clearly, the $(TiO_2)_5$ cluster always shows the largest deformation when a composite system is formed. Indeed, a quite linear trend emerges ($R$ = 0.78) when plotting $E_{ads}$ *versus* $E_{def}$ $(TiO_2)_5$ as depicted in Fig. 2. Here, three different regions are delimited: (i) high $E_{def}$ and $E_{ads}$; (ii) intermediate $E_{def}$ and $E_{ads}$; and (iii) low $E_{def}$ and $E_{ads}$, corresponding to titania/MXene composites where the MXene (0001) surface is composed of $d^3$, $d^4$, and $d^5$ transition metal. In short, the formation of titania/MXene composites induces a large reconstruction of the titania cluster.

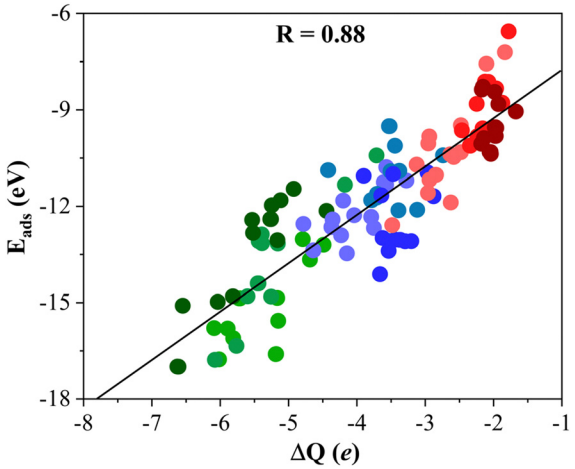


Fig. 4 Linear trend between $E_{ads}$ and $\Delta Q$ of the titania cluster. The solid black line is the linear correlation between both quantities, and $R$ stands for the regression coefficient. Color-coding as in Fig. 3. Linear fitting analysis is reported in Table S12 of the ESI.†

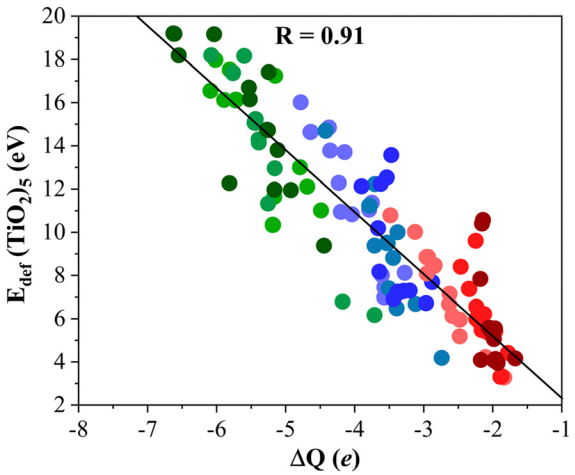


Fig. 5 Linear correlation between $E_{def}$ $(TiO_2)_5$ and $\Delta Q$. Solid black line is the linear correlation between both quantities, while $R$ stands for the linear correlation regression coefficient. Color coding as in Fig. 3. Linear fitting analysis is reported in Table S12 of the ESI.†

Open Access Article. Published on 22 July 2024. Downloaded on 7/9/2025 8:47:37 PM.
This article is licensed under a Creative Commons Attribution-NonCommercial 3.0 Unported Licence.

From a structural point of view, the fully relaxed geometries of the most exothermic configurations of each composite before and after adsorption are presented in Fig. 1 and 3, respectively. Fig. 3 clearly and consistently shows a deformation of titania clusters upon adsorption over $M_2C$ (0001) surfaces, in agreement with the above analyzed deformation energies. In fact, titania clusters are adsorbed in equivalent positions over $M_2C$ composed of $d^3$ and $d^4$ metals according to the inherent hexagonal symmetry of $M_2C$ (0001) surfaces and seem to follow the ABC MXene stacking. Despite titania clusters being adsorbed in different positions over $M_2C$ involving $d^5$ metals, all titania clusters, regardless of the $M_2C$ metal composition, present O atoms in contact with the $M_2C$ surfaces occupying the high-symmetry adsorption sites (mainly hollow ones) upon adsorption. Indeed, some O atoms change plane in the cluster to maximize the number of contacts between the cluster and the surfaces and occupy the mentioned sites. Further structural analysis concerning atomic distances and angles are reported in Fig. S1 of the ESI.† The initial geometry found in the gas phase configuration of the $(TiO_2)_5$ cluster is lost when it is anchored on the MXene support.

### 3.2. Chemical bonding analysis of $(TiO_2)_5/M_2C$ composites

To gain further insight into the formation of titania/MXene composites depicted in Fig. 3, we conduct a topological analysis of the electron density to obtain Bader charges, and analyze CDD and PA-CDD plots, to investigate electron transfer between the components. Table 1 compiles $\Delta Q$ of the supported $(TiO_2)_5$ cluster resulting from Bader analysis. These data correspond to the most stable configuration for each MXene, while data for other configurations are reported in the ESI.† The $\Delta Q$ values in Table 1 represent the difference between the net charge on

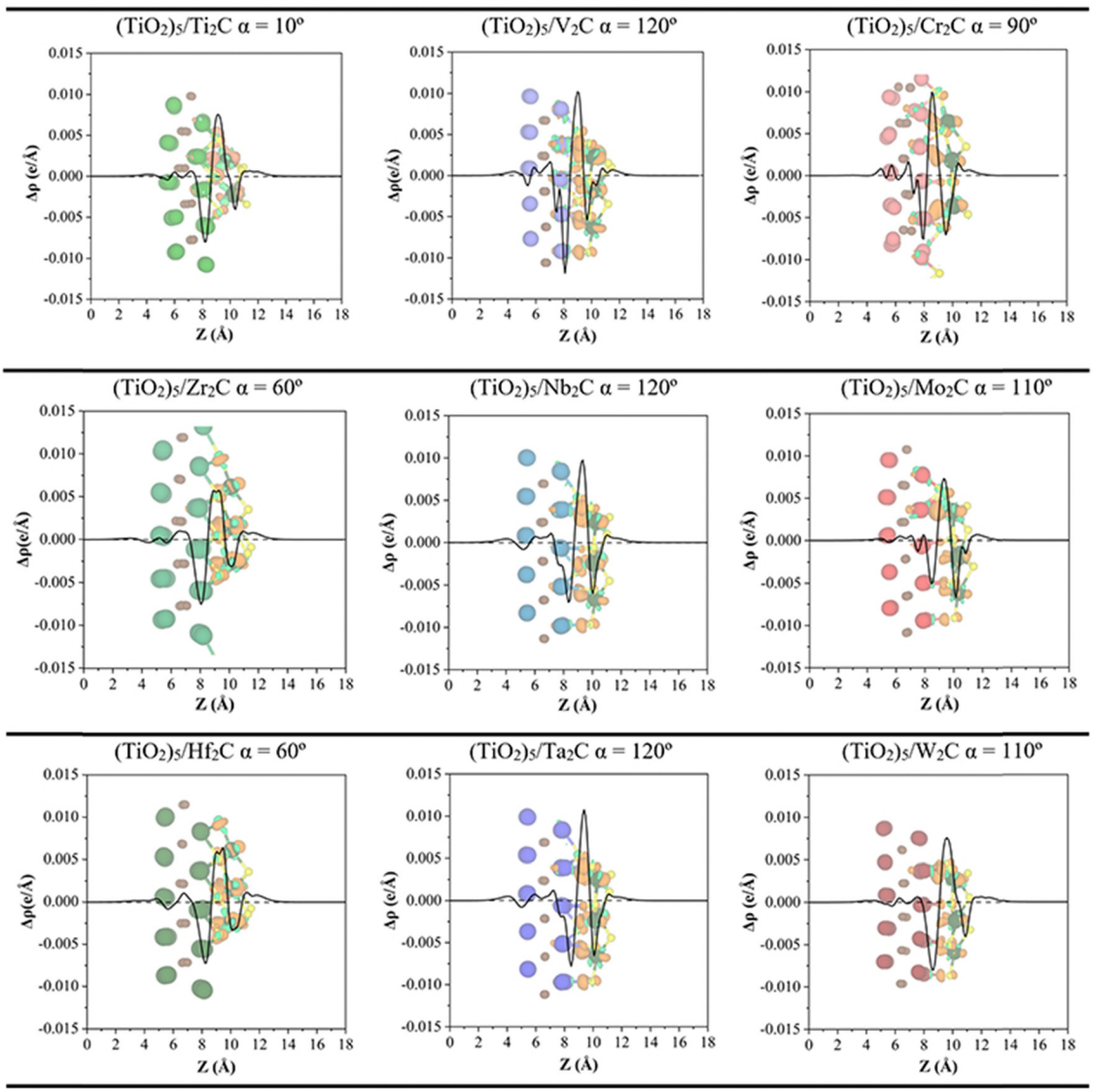


Fig. 6 Plane-averaged charge density difference (PA-CDD) $\Delta\rho$ along the direction normal to the MXene surface, $Z$, for the most stable configurations of $M_2C/(TiO_2)_5$ as listed in Table 1. Charge density differences, CDD, with an isosurface value of 0.015 e $Å^{-3}$, are depicted inset where pale green and orange isosurfaces correspond to accumulation and depletion charges, respectively. Color coding as in Fig. 3.

 This journal is © the Owner Societies 2024

Open Access Article. Published on 22 July 2024. Downloaded on 7/9/2025 8:47:37 PM.
This article is licensed under a Creative Commons Attribution-NonCommercial 3.0 Unported Licence.

the titania nanocluster before and after adsorption. Since the isolated titania cluster is neutral, a negative $\Delta Q$ means the electron accumulation on the supported titania nanocluster. Thus, $\Delta Q < 0$ implies an electron density excess on the supported cluster resulting from electron transfer from the $M_2C$ (0001) MXene surface towards the $(TiO_2)_5$ cluster. This electron excess is likely to promote the activation of the supported particle although further work involving study of the reactivity of the supported cluster is required to confirm this hypothesis. The electron density flow towards the titania cluster is systematically observed in all possible configurations regardless of the MXene composition, see Tables S1–S9 in the ESI.† $\Delta Q$ runs between −2.04 and −6.62 $e$ and follows a similar trend as observed in $E_{ads}$, confirming that a large adsorption energy is coupled with a large charge transfer, as shown in Fig. 4. The electron density accumulation at or near the $(TiO_2)_5$ cluster is accompanied by electron density depletion at the MXene surface. Usually, the excess electron density of an adsorbate results in structural changes. The case of the $CO_2$ molecule interacting with MXenes is a clear example as the electron transfer towards $CO_2$ promotes a considerable bending of the adsorbed molecule.[54,55] To explore this effect in more detail, Fig. 5 plots $E_{def}$ $(TiO_2)_5$ *vs.* $\Delta Q$ of the supported titania cluster. This plot exhibits a quite clear linear trend ($R$ = 0.91) that the charge transfer is the driving force that promotes the titania cluster deformation.

In addition, the CDD and the PA-CDD plots along the surface normal direction are presented in Fig. 6 for the most favorable composites (see Table 1 and Fig. 3). These plots complement the Bader analysis as they provide a visualization of the charge rearrangement induced by the formation of the composites. In all cases, a depletion of charge density is observed at the MXene M atoms and accumulation, at the Ti atoms from the $(TiO_2)_5$ cluster, consistent with previous work.[41] The inset CDD plots in Fig. 6 show a clear redistribution of the electron density in the interface region. Altogether, both plots demonstrate that the electron density is mainly depleted in the MXene while it mainly accumulates in the $(TiO_2)_5$ cluster, in agreement with Bader charges. The strong charge transfer from MXene towards the $(TiO_2)_5$ cluster implies a high contribution of ionic bonding, however, the DOS projected per atomic orbital from Fig. S2 in the ESI† also shows a large mixing of orbitals, in this case, typical of a covalent bond. These two facts allow us to conclude that the chemical bond can be described as a mixture of covalent and ionic bonding. Furthermore, this electron transfer from the $M_2C$ MXene to $(TiO_2)_5$ clusters could generate a build-in electric field near the interface that can be beneficial in photocatalytic applications acting as a separator of charge carriers.[56]

Further analysis is performed through the investigation of the work function, $\Phi$, of each $M_2C$ MXene. One would, in general, expect that the lower the $\Phi$, the easier the electron donation to the adsorbed titania cluster. Looking at the results reported in Table 1, the MXenes with the lowest $\Phi$ correspond to those composed of $d^3$ transition metals followed by $d^4$ and $d^5$ ones. Indeed, the emerging trends when plotting $E_{ads}$ or $E_{def}$ $(TiO_2)_5$ *versus* $\Phi$ (*cf.* Fig. 7a and b) are analogous to those in Fig. 4 and 5. This is also consistent with the plot of $\Phi$ *versus* $\Delta Q$ in Fig. 7c indicating that, as expected, the electron transfer increased when $\Phi$ decreased, indeed with a relatively high regression coefficient, $R$, of 0.83.

### 3.3. Generalized trends of $(TiO_2)_5/M_2C$ composites

The main structural differences of these composites reside in the metal of the MXene. Hence, it is logical to investigate

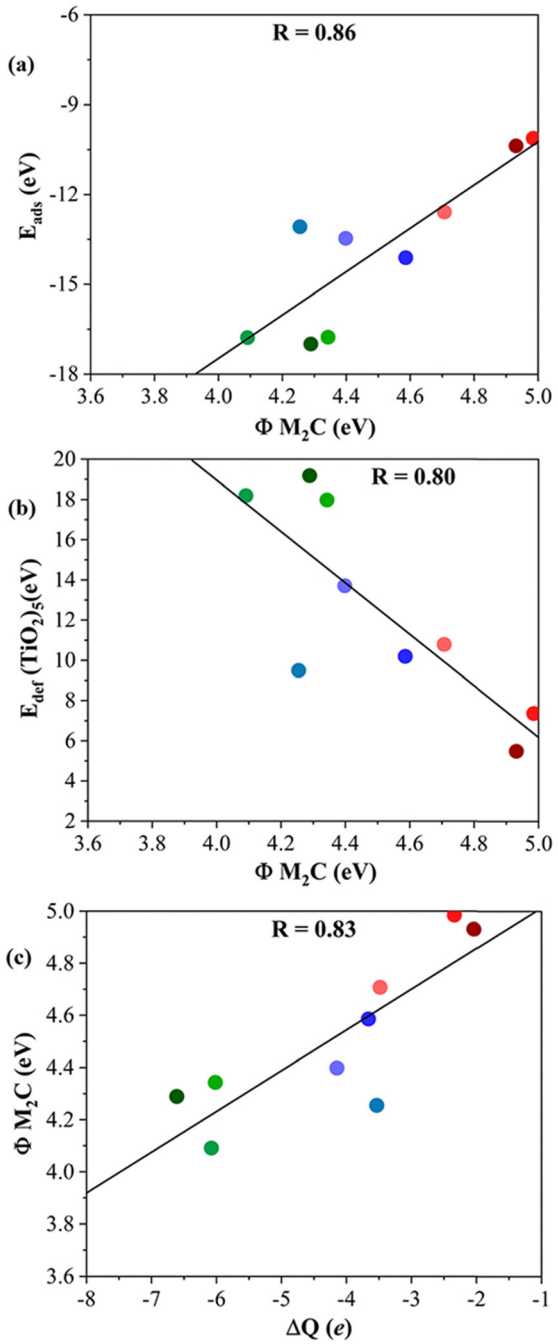


Fig. 7 (a) $E_{ads}$ *vs.* the work function, $\Phi$, of bare (0001) MXene surfaces; (b) $E_{def}$ $(TiO_2)_5$ *vs.* $\Phi$ $M_2C$; and (c) $\Phi$ $M_2C$ *vs.* $\Delta Q$ of $(TiO_2)_5$. The solid black lines correspond to the linear fitting associated with the regression coefficient, $R$. Color coding as in Fig. 3. Linear fitting analysis is reported in Table S12 of the ESI.†

Open Access Article. Published on 22 July 2024. Downloaded on 7/9/2025 8:47:37 PM.
This article is licensed under a Creative Commons Attribution-NonCommercial 3.0 Unported Licence.

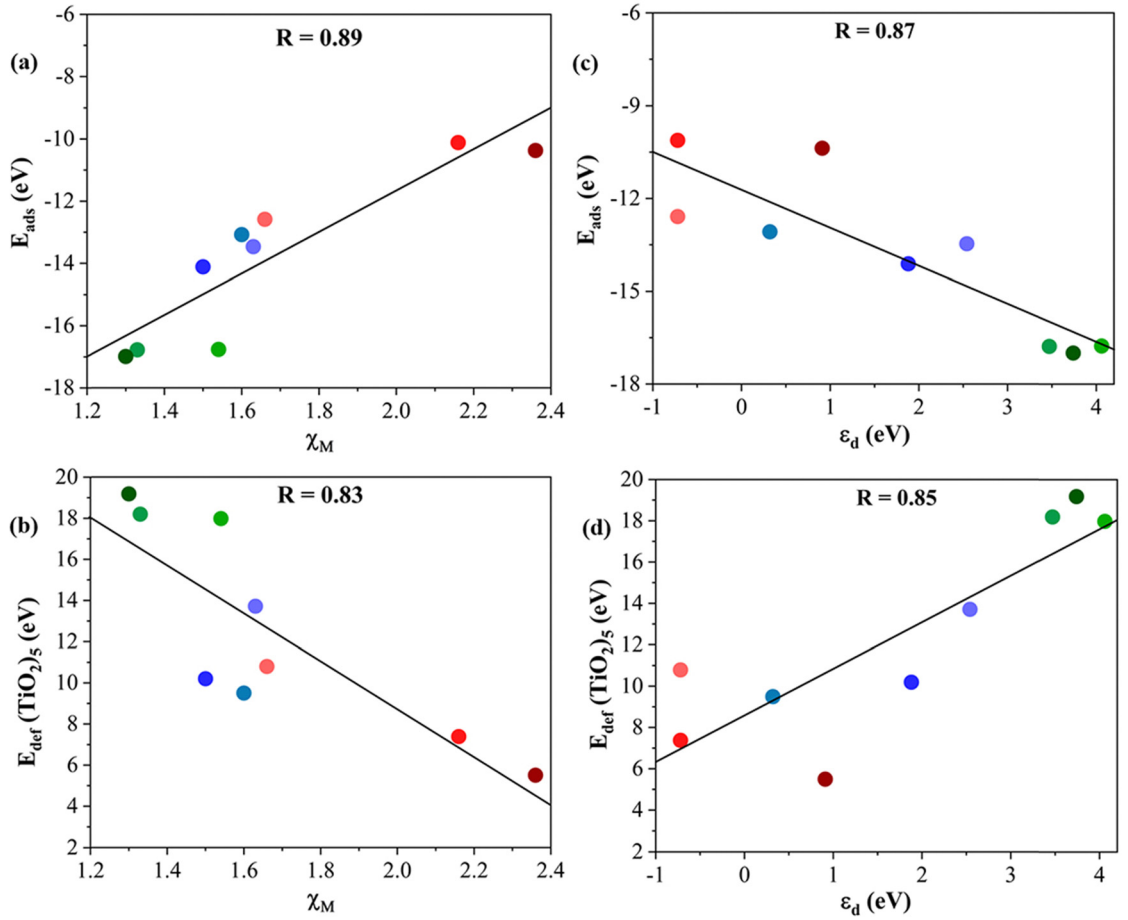


Fig. 8 Tentative linear correlations of (a) $E_{ads}$ *vs.* $\chi_M$, (b) $E_{def}$ $(TiO_2)_5$ *vs.* $\chi_M$, (c) $E_{ads}$ *vs.* $\varepsilon_d$, and (d) $E_{def}$ $(TiO_2)_5$ *vs.* $\varepsilon_d$. The linear regression coefficient, *R*, is given in the inset in each panel. Color coding as in Fig. 3. Linear fitting analysis is reported in Table S12 of the ESI.†

descriptors characteristic of transition metals such as the metal atom electronegativity, $\chi_M$ and the d-band center, $\varepsilon_d$, of the metal in the MXene structure.[57] In particular, we focus on whether these descriptors would help tentatively predict the $E_{ads}$ and the $E_{def}$ $(TiO_2)_5$ of a given $M_2C$ MXene. Fig. 8 shows clear linear correlations associated with the most favorable $(TiO_2)_5/M_2C$ composites listed in Table 1. Starting with the $\chi_M$ descriptor (*cf.* Fig. 8a and b), the adsorption energy increases as $\chi_M$ decreases. Thus, MXenes involving a $d^3$ transition metal interact more strongly with the $(TiO_2)_5$ cluster than those MXene composed of $d^4$ or $d^5$ metal. This is consistent with the large $E_{def}$ $(TiO_2)_5$ observed in MXene composed of $d^3$ metals. In summary, we can conclude that $(TiO_2)_5/M_2C$ composites involving transition metals with a relatively low $\chi_M$ will exhibit a large exothermic interaction between the two constituents and a large structural modification on the $(TiO_2)_5$ nanoclusters.

The trends corresponding to the second analyzed descriptor, $\varepsilon_d$, are depicted in Fig. 8c and d which also exhibit a reasonable linear trend. In general, MXenes involving a transition metal with a high $\varepsilon_d$ lead to large exothermic adsorption energy and large deformation energy on $(TiO_2)_5$ nanoclusters. Based on the aforementioned analysis, $\chi_M$ and $\varepsilon_d$ can be considered feasible descriptors to predict the formation of titania/MXene composites based on the MXene composition.

## 4. Conclusions

The formation of titania/MXene composites obtained by supporting a $(TiO_2)_5$ cluster on the basal surface of $M_2C$ MXenes with M = Ti, Zr, Hf, V, Nb, Ta, Cr, Mo, and W has been investigated by means of periodic DFT based calculation on appropriate supercells. The present results systematically show a highly exothermic adsorption energy. The MXenes involving $d^3$ metals (Ti, Zr, and Hf) have the largest interaction followed by $d^4$ (V, Nb, Ta) and $d^5$ (Cr, Mo, and W) metals. The composite formation involved an important change in the atomic structure of the supported $(TiO_2)_5$ cluster, relative to the most stable gas phase conformation in such a way that the largest adsorption promotes the largest deformation. The analysis of Bader charge and CDD plots shows a clear electron transfer from the MXene towards the $(TiO_2)_5$ cluster. The accumulation of electron density in the supported $(TiO_2)_5$ cluster is at the origin of its deformation.

 This journal is © the Owner Societies 2024

Open Access Article. Published on 22 July 2024. Downloaded on 7/9/2025 8:47:37 PM.
This article is licensed under a Creative Commons Attribution-NonCommercial 3.0 Unported Licence.

These systematic trends are rationalized using the MXene work function, the electronegativity of the metal atom, and the d-band center of the metal in the MXene. MXenes with a low work function are those that show high adsorption energy with a concomitant high deformation energy of the $(TiO_2)_5$ cluster and a large electron transfer. MXenes composed of metals with low electronegativity show high adsorption energies including the high deformation energy of the $(TiO_2)_5$ nanocluster and high electron transfer. Finally, the higher the d-band center of the metal in the MXene, the higher the adsorption and deformation energies and also the electron transfer. Finally, it has been shown that features of the metal element in the MXene can be used to predict trends in the interaction and in the extent of electron transfer when forming titania/MXene composites, valuable information for experimentalists interested in the synthesis, properties, and possible applications of these composites.

## Data availability

The data supporting this article have been included as part of the ESI.†

## Conflicts of interest

There are no conflicts to declare.

## Acknowledgements

This study has been supported by the Spanish Ministerio de Ciencia e Innovación and Agencia Estatal de Investigación (AEI) MCIN/AEI/10.13039/501100011033 through projects PID2020-115293RJ-I00, PID2021-126076NB-I00, TED2021-129506B-C22, la Unidad de Excelencia María de Maeztu CEX2021-001202-M granted to the IQTCUB and, in part, from COST Action CA18234, and Generalitat de Catalunya 2021SGR00079. N. G.-R. thanks the Generalitat de Catalunya for a predoctoral contract 2022 FISDU 00106. F. V. is thankful for the ICREA Academia Award 2023 Ref. Ac2216561.

## References

1 A. Fujishima and K. Honda, *Nature*, 1972, **238**, 37–38.
2 N. Serpone and A. V. Emeline, *J. Phys. Chem. Lett.*, 2012, **3**, 673–677.
3 B. Samanta, Á. Morales-García, F. Illas, N. Goga, J. A. Anta, S. Calero, A. Bieberle-Hütter, F. Libisch, A. B. Muñoz-García, M. Pavone and M. C. Toroker, *Chem. Soc. Rev.*, 2022, **51**, 3794–3818.
4 P. K. J. Robertson, J. M. C. Robertson and D. W. Bahnemann, *J. Hazard. Mater.*, 2012, **211–212**, 161–171.
5 D. Zhu and Q. Zhou, *Environ, Nanotechnol. Monit.*, 2019, **12**, 100255.
6 T. Hisatomi and K. Domen, *Nat. Catal.*, 2019, **2**, 387–399.
7 X. Jiao, K. Zheng, L. Liang, X. Li, Y. Sun and Y. Xie, *Chem. Soc. Rev.*, 2020, **49**, 6592–6604.
8 E. Kozlova, A. Safatov, S. Kiselev, V. Y. Marchenko, A. Sergeev, M. Skarnovich, E. Emelyanova, M. Smetannikova, G. Buryak and A. Vorontsov, *Environ. Sci. Technol.*, 2010, **44**, 5121–5126.
9 Y. Li, Y.-K. Peng, L. Hu, J. Zheng, D. Prabhakaran, S. Wu, T. J. Puchtler, M. Li, K.-Y. Wong and R. A. Taylor, *Nat. Commun.*, 2019, **10**, 4421.
10 A. Shahzad, K. Rasool, M. Nawaz, W. Miran, J. Jang, M. Moztahida, K. A. Mahmoud and D. S. Lee, *Chem. Eng. J.*, 2018, **349**, 748–755.
11 Y. Zhao, N. Liu, S. Zhou and J. Zhao, *J. Mater. Chem. A*, 2019, **7**, 16294–16303.
12 D. O. Scanlon, C. W. Dunnill, J. Buckeridge, S. A. Shevlin, A. J. Logsdail, S. M. Woodley, C. R. A. Catlow, M. J. Powell, R. G. Palgrave and I. P. Parkin, *Nat. Mater.*, 2013, **12**, 798–801.
13 M. A. Henderson, *Surf. Sci. Rep.*, 2011, **66**, 185–297.
14 Y. Yamada and Y. Kanemitsu, *Appl. Phys. Lett.*, 2012, **101**, 133907.
15 R. Reichert, Z. Jusys and R. J. Behm, *J. Phys. Chem. C*, 2015, **119**, 24750–24759.
16 X. Wang, Y. Ruan, S. Feng, S. Chen and K. Su, *ACS Sustainable Chem. Eng.*, 2018, **6**, 11424–11432.
17 Y. Chen, Ll Soler, C. Cazorla, J. Oliveras, N. G. Bastús, V. F. Puntes and J. Llorca, *Nat. Commun.*, 2023, **14**, 6165.
18 M. Allès, E. R. Remesal, F. Illas and Á. Morales-García, *Adv. Theory Simul.*, 2023, **10**, 2200670.
19 C. Di Valentin, E. Finazzi, G. Pacchioni, A. Selloni, S. Livraghi, M. C. Paganini and E. Giamello, *Chem. Phys.*, 2007, **339**, 44–56.
20 E. R. Remesal and Á. Morales-García, *Phys. Chem. Chem. Phys.*, 2022, **24**, 21381–21387.
21 E. R. Remesal, Á. Morales-García and F. Illas, *J. Phys. Chem. C*, 2023, **127**, 20128–20136.
22 C. Di Valentin, G. Pacchioni, A. Selloni, S. Livraghi and E. Giamello, *J. Phys. Chem. B*, 2005, **109**, 11414–11419.
23 M. Naguib, M. Kurtoglu, V. Presser, J. Lu, J. Niu, M. Heon, L. Hultman, Y. Gogotsi and M. W. Barsoum, *Adv. Mater.*, 2011, **23**, 4248–4253.
24 J. Low, L. Zhang, T. Tong, B. Shen and J. Yu, *J. Catal.*, 2018, **361**, 255–266.
25 Á. Morales-García, F. Calle-Vallejo and F. Illas, *ACS Catal.*, 2020, **10**, 13487–13503.
26 D. Dolz, R. De Armas, P. Lozano-Reis, Á. Morales-García, R. Sayós and F. Illas, *ChemCatChem*, 2024, DOI: **10.1002/cctc.202400122**.
27 H. Zhou, Z. Chen, E. Kountoupi, A. Tsoukalou, P. M. Abdala, P. Florian, A. Fedorov and C. R. Müller, *Nat. Commun.*, 2021, **12**, 5510.
28 A. Jurado, Á. Morales-García, F. Viñes and F. Illas, *ACS Catal.*, 2022, **12**, 15658–15667.
29 S. Kazim, C. Huang, N. H. Hemasiri, A. Kulkarni, S. Mathur and S. Ahmad, *Adv. Funct. Mater.*, 2024, 2315694, DOI: **10.1002/adfm.202315694**.

Open Access Article. Published on 22 July 2024. Downloaded on 7/9/2025 8:47:37 PM.
This article is licensed under a Creative Commons Attribution-NonCommercial 3.0 Unported Licence.

30 A. Dey, S. Varagnolo, N. P. Power, N. Vangapally, Y. Elias, L. Damptey, B. N. Jaato, S. Gopalan, Z. Golrokhi, P. Sonar, V. Selvaraj, D. Aurbach and S. Krishnamurthy, *Prog. Mater. Sci.*, 2023, **139**, 101166.
31 G. Gao, A. P. O'Mullane and A. Du, *ACS Catal.*, 2017, **7**, 494–500.
32 Z. Guo, J. Zhou, L. Zhu and Z. Sun, *J. Mater. Chem. A*, 2016, **4**, 11446–11452.
33 D. Ontiveros, F. Viñes and C. Sousa, *J. Mater. Chem. A*, 2023, **11**, 13754–13764.
34 J. Chen, H. Zheng, Y. Zhao, M. Que, W. Wang and X. Lei, *Ceram. Int.*, 2020, **46**, 20088–20096.
35 S. Debow, T. Zhang, X. Liu, F. Song, Y. Qian, J. Han, K. Maleski, Z. B. Zander, W. R. Creasy and D. L. Kuhn, *J. Phys. Chem. C*, 2021, **125**, 10473–10482.
36 L. Jiao, C. Zhang, C. Geng, S. Wu, H. Li, W. Lv, Y. Tao, Z. Chen, G. Zhou and J. Li, *Adv. Energy Mater.*, 2019, **9**, 1900219.
37 R. Li, X. Ma, J. Li, J. Cao, H. Gao, T. Li, X. Zhang, L. Wang, Q. Zhang and G. Wang, *Nat. Commun.*, 2021, **12**, 1587.
38 M. M. Nair, A. C. Iacoban, F. Neatu, M. Florea and S. Neatu, *J. Mater. Chem. A*, 2023, **11**, 12559–12592.
39 S. A. Khan, B. Amin, L.-Y. Gan and I. Ahmad, *Phys. Chem. Chem. Phys.*, 2017, **19**, 14738–14744.
40 L. Xu, T. Wu, P. R. Kent and D.-E. Jiang, *Phys. Rev. Mater.*, 2021, **5**, 054007.
41 N. García-Romeral, M. Keyhanian, Á. Morales-García, F. Viñes and F. Illas, *Chem. Eur. J.*, 2024, **30**, e202400255.
42 O. Lamiel-García, A. Cuko, M. Calatayud, F. Illas and S. T. Bromley, *Nanoscale*, 2017, **9**, 1049–1058.
43 Á. Morales-García, R. Valero and F. Illas, *J. Chem. Theory Comput.*, 2017, **13**, 3746–3753.
44 G. Kresse and J. Furthmüller, *Comput. Mater. Sci.*, 1996, **6**, 15–50.
45 G. Kresse and J. Furthmüller, *Phys. Rev. B: Condens. Matter Mater. Phys.*, 1996, **54**, 11169.
46 P. E. Blöchl, *Phys. Rev. B: Condens. Matter Mater. Phys.*, 1994, **50**, 17953.
47 J. P. Perdew, K. Burke and M. Ernzerhof, *Phys. Rev. Lett.*, 1996, **77**, 3865.
48 H. J. Monkhorst and J. D. Pack, *Phys. Rev. B: Condens. Matter Mater. Phys.*, 1976, **13**, 5188.
49 R. F. W. Bader, *Atoms in Molecules: A Quantum Theory*, Clarendon Press, 1994.
50 W. Tang, E. Sanville and G. Henkelman, *J. Phys.: Condens. Matter*, 2009, **21**, 084204.
51 V. Wang, N. Xu, J.-C. Liu, G. Tang and W.-T. Geng, *Comput. Phys. Commun.*, 2021, **267**, 108033.
52 G. Di Liberto, Á. Morales-García and S. T. Bromley, *Nat. Commun.*, 2022, **13**, 6236.
53 H. Oschinski, Á. Morales-García and F. Illas, *J. Phys. Chem. C*, 2021, **125**, 2477–2484.
54 Á. Morales-García, A. Fernández-Fernández, F. Viñes and F. Illas, *J. Mater. Chem. A*, 2018, **6**, 3381–3385.
55 R. Morales-Salvador, Á. Morales-García, F. Viñes and F. Illas, *Phys. Chem. Chem. Phys.*, 2018, **20**, 17117–17124.
56 M.-L. Tsai, S.-H. Su, J.-K. Chang, D.-S. Tsai, C.-H. Chen, C.-I. Wu, L.-J. Li, L.-J. Chen and J.-H. He, *ACS Nano*, 2014, **8**, 8317–8322.
57 B. M. Abraham, O. Piqué, M. A. Khan, F. Viñes, F. Illas and J. K. Singh, *ACS Appl. Mater. Interfaces*, 2023, **15**, 30117–30126.